

MODELING OF LYMAN-ALPHA EMITTING GALAXIES AND IONIZED BUBBLES AT THE ERA OF REIONIZATION

HIDENOBU YAJIMA^{1,2}, KAZUYUKI SUGIMURA², KENJI HASEGAWA³,

¹Frontier Research Institute for Interdisciplinary Sciences, Tohoku University, Sendai, Miyagi 980-8578, Japan

²Astronomical Institute, Tohoku University, Sendai, Miyagi 980-8578, Japan and

³Graduate School of Science, Nagoya University, Furo-cho, Chikusa-ku, Nagoya, Aichi 464-8602, Japan

Draft version January 23, 2017

ABSTRACT

Understanding Ly α emitting galaxies (LAEs) can be a key to reveal cosmic reionization and galaxy formation in the early Universe. Based on halo merger trees and Ly α radiation transfer calculations, we model redshift evolution of LAEs and their observational properties at $z \geq 6$. We consider ionized bubbles associated with individual LAEs and IGM transmission of Ly α photons. We find that Ly α luminosity tightly correlates with halo mass and stellar mass, while the relation with star formation rate has a large dispersion. Comparing our models with the observed luminosity function by Konno et al. (2014), we suggest that LAEs at $z \sim 7$ have galactic wind of $V_{\text{out}} \gtrsim 150 \text{ km s}^{-1}$ and HI column density of $N_{\text{HI}} \gtrsim 10^{20} \text{ cm}^{-2}$. Number density of bright LAEs rapidly decreases as redshift increases, due to both lower star formation rate and smaller HII bubbles. Our model predicts future wide deep surveys with next generation telescopes, such as JWST, E-ELT and TMT, can detect LAEs at $z \sim 10$ with a number density of $n_{\text{LAE}} \sim \text{a few} \times 10^{-6} \text{ Mpc}^{-3}$ for the flux sensitivity of $10^{-18} \text{ erg cm}^{-2} \text{ s}^{-1}$. By combining these surveys with future 21-cm observations, it could be possible to detect both LAEs with $L_{\text{Ly}\alpha} \gtrsim 10^{42} \text{ erg s}^{-1}$ and their associated giant HII bubbles with the size $\gtrsim 250 \text{ kpc}$ at $z \sim 10$.

Subject headings: radiative transfer – line: profiles – galaxies: evolution – galaxies: formation – galaxies: high-redshift

1. INTRODUCTION

One of the major challenges in today’s astronomy is revealing cosmic reionization history with galaxy evolution. Recent CMB observations suggested cosmic reionization occurred at $z \sim 8 - 11$ (Komatsu et al. 2011; Planck Collaboration et al. 2014, 2016). Gunn-Peterson tests by the observations of high-redshift QSOs indicated cosmic reionization completed at $z \sim 6$ (e.g., Fan et al. 2006). However, the ionization history of integer-galactic medium (IGM) has not been understood yet. Recent observations of high-redshift galaxies at $z \gtrsim 7$ are gradually unveiling the cosmic star formation history (Ouchi et al. 2010; Bouwens et al. 2012, 2015; Oesch et al. 2015, 2016), and have allowed us to speculate the cosmic reionization history (Robertson et al. 2015). Yet, even considering the above observational constraints, various reionization histories remain viable (Cen 2003; Yajima & Khochfar 2015). One of the main uncertainties is low-mass galaxy formation with the halo mass M_{h} less than $\sim 10^{12} M_{\odot}$. Due to their higher number density and the higher escape fraction of ionizing photons from them (Razoumov & Sommer-Larsen 2010; Paardekooper et al. 2013; Yajima et al. 2011, 2014), low-mass galaxies can be responsible for main ionizing sources. However, the detection sensitivities of current observations are not sufficient to constrain the formation of low-mass galaxies. Therefore it is important to theoretically investigate the formation of low-mass galaxies and their contribution to cosmic reionization.

Most of high-redshift low-mass galaxies are observed as Ly α emitters (LAEs; Hu & McMahon 1996; Steidel et al.

2000; Iye et al. 2006; Gronwall et al. 2007; Ouchi et al. 2008, 2010; Bond et al. 2011; Ciardullo et al. 2012; Yamada et al. 2012). Ouchi et al. (2010) indicated that LAEs were hosted in halos with the halo mass $M_{\text{h}} \sim 10^{11} M_{\odot}$ by the clustering analysis (see also, Gawiser et al. 2007). Verhamme et al. (2008) suggested that LAEs were not dust-enriched well yet so that Ly α photons escaped from galaxies against dust attenuation (see also, Yajima et al. 2014). These suggest LAEs are likely to be in the early phase of galaxy evolution (e.g., Mori & Umemura 2006). In addition, LAEs are one of major populations of galaxies contributing the cosmic star-formation density in the early Universe (Ciardullo et al. 2012).

LAEs also have been used as a tool to investigate the early Universe (Iye et al. 2006; Vanzella et al. 2011; Ono et al. 2012; Shibuya et al. 2012; Finkelstein et al. 2013; Zitrin et al. 2015; Song et al. 2016b). Number density of LAEs rapidly decreases at $z \gtrsim 7$ (Ono et al. 2012; Konno et al. 2014), indicating that Ly α fluxes from some galaxies were significantly attenuated due to neutral hydrogen in the IGM (e.g., Kashikawa et al. 2006). Meanwhile, LAEs themselves could provide sufficient ionizing photons into the IGM (Yajima et al. 2009, 2014), and some of them could make giant HII bubbles that allowed Ly α photons to reach us. In this case, galaxies can be observed as LAEs. In practice, the most distant LAE has been observed even at $z = 8.68$ (Zitrin et al. 2015). Thus, LAEs can be the key objects in understanding the galaxy formation and cosmic reionization.

In this work, we investigate the evolution of LAEs with their associated HII bubbles. By modeling both LAEs and HII bubbles simultaneously, we estimate Ly α lumi-

osity functions (LFs), number density of LAEs, size distribution of HII bubbles, and the relation between Ly α flux and the size of HII bubble. These estimations are useful for future observational missions. James Webb Space Telescope (JWST) is going to be launched at 2018, and aims to observe galaxies at $z \sim 10$. Its high sensitivity of spectroscopy will make it possible to detect Ly α flux from galaxies if they distribute in giant HII bubbles. Later on, 30-m class ground telescopes, the European Extremely Large Telescope (E-ELT), the Thirty Meter Telescope (TMT), and the Giant Magellan Telescope (GMT), will investigate galaxies at $z \sim 10$ statistically. In addition, several 21-cm observational missions are on going, e.g., the LOw Frequency ARray (LOFAR; Harker et al. 2010), and Murchison Widefield Array (MWA; Lonsdale et al. 2009). In future, Square Kilometer Array phase-2 (SKA-2; Dewdney et al. 2009) will perform large-scale 21-cm tomography. Since 21-cm emission comes from HI gas, detections of holes of 21-cm signal indicate giant HII bubbles around galaxies. Therefore, a combination of 21-cm and galaxy observations will provide fruitful information about the cosmic reionization and galaxy formation (e.g., Lidz et al. 2009).

Theoretically large-scale simulations showed that galaxies made patchy ionization structures in an inside-out fashion (e.g., Iliiev et al. 2006, 2012; Mellema et al. 2006; Trac & Cen 2007; Ocvirk et al. 2016), whereas low-density void regions would be ionized first, in the so-called outside-in fashion, if AGNs were the main ionizing sources. However, AGNs are unlikely to be main ionizing sources because of the rapid decrease of observed number density at redshift $z > 4$ (e.g., Richards et al. 2006), although the contribution of faint AGNs is still under the debate (Madau & Haardt 2015; Yoshiura et al. 2016). Thus, in this paper, we model LAEs assuming the reionization model with the inside-out fashion. In order to understand cosmic reionization theoretically, we need high spatial resolution to follow the detailed physical processes of interstellar medium, as well as large volume to consider large-scale inhomogeneity of ionization structure. Even current numerical simulations cannot resolve such a wide dynamic range. For that reason, in this work, we semi-analytically investigate the cosmic reionization and galaxy formation based on simple structure formation models and radiative transfer calculations. We use the cosmological parameters, $\Omega_\Lambda = 0.7$, $\Omega_M = 0.3$, $\Omega_b = 0.045$ and $h = 0.7$ (Komatsu et al. 2011; Planck Collaboration et al. 2016).

The paper is organized as follows. We describe our models of star formation and HII bubbles in §2. In §3, we present the results, which include the Ly α properties, LFs of LAEs and redshift evolution of number density of LAEs. We discuss the relation between the Ly α flux of galaxies and the sizes of HII bubbles in §5, and summarize in §6.

2. MODEL

In the current standard picture of structure formation, halos grow via minor/major mergers. In our model, the star formation rate (SFR) in a halo is assumed to be proportional to the growth rate of the halo as follows:

$$\text{SFR} = \frac{dM_{\text{star}}}{dt} = \frac{dM_{\text{star}}}{dM_h} \frac{dM_h}{dt}. \quad (1)$$

The relation between stellar and halo mass can be written as $\frac{dM_{\text{star}}}{dM_h} = \frac{d \log M_{\text{star}}}{d \log M_h} \frac{M_{\text{star}}}{M_h}$. The abundance matching analysis by Behroozi et al. (2013) indicated that $\frac{d \log M_{\text{star}}}{d \log M_h} \sim \text{const}$ for $M_h \lesssim 10^{12} M_\odot$. In addition, Behroozi & Silk (2015) showed the weak dependence of $\frac{M_{\text{star}}}{M_h}$ on halo mass and redshift at the mass range $M_h \sim 10^{11} - 10^{13} M_\odot$, although $\frac{M_{\text{star}}}{M_h}$ increases with M_h at $M_h \lesssim 10^{11} M_\odot$ (see also, Moster et al. 2013; Kravtsov et al. 2014). Therefore we here assume $\frac{dM_{\text{star}}}{dM_h} \sim \text{const}$. Thus, we estimate SFR from the growth rate of halo mass with a constant tuning parameter α , i.e., $\text{SFR} = \alpha \frac{dM_h}{dt}$. In order to estimate the growth of halos, we use halo merger trees based on an extended Press-Schechter formalism (Somerville & Kolatt 1999; Khochfar & Burkert 2001, 2006). The halo merger trees include 5000 realizations with the halo mass range of $10^9 - 10^{13} M_\odot$ at $z = 6$. In this work, we allow star formation only for halos with the mass $M_h > 10^8 M_\odot$, because star formation in less massive halos can be significantly suppressed due to UV background or internal stellar feedback (e.g., Okamoto et al. 2008; Hasegawa & Semelin 2013). In deriving statistical properties, e.g., cosmic SFR density, stellar mass density and LF, we sum the contribution of each merger tree with normalization factors that reproduce the halo mass function of Sheth & Tormen (2002). We determine the tuning parameter by using observed cosmic SFR density and stellar mass density at $z \sim 7 - 8$. Figure 1 shows our modeled SFR and stellar mass density with observations. We choose the parameter α by the least square fitting to the four points of the observations. The observed SFR and stellar mass densities consider only galaxies with $M_{\text{UV}} < -17$ and $M_{\text{star}} \geq 10^8 M_\odot$, respectively. Therefore, we consider only the galaxies satisfying the above criteria for the fitting. The best fit value is $\alpha = 3.3 \times 10^{-3}$. Note that, so far there is no available data about $\frac{dM_{\text{star}}}{dM_h}$ at $z \gtrsim 9$ and α can change with halo mass and redshift. However, for simplicity, we assume α is constant. Following the above way, we derive star formation history from each halo merger tree.

We also derive UV LFs by converting SFR to UV flux with $L_{\nu, \text{UV}} = 0.7 \times 10^{28} \text{ erg s}^{-1} \left(\frac{\text{SFR}}{1 M_\odot \text{ yr}^{-1}} \right)$ (Madau et al. 1999). Figure 2 shows our modeled LFs at $z \sim 7$ and ~ 8 with those from the recent observation by Bouwens et al. (2015). The observation indicated that a part of UV flux are absorbed by dust with the escape fraction $f_{\text{esc, UV}} \sim 0.6$. Our modeled LFs match the observation well with the same UV escape fraction.

Galaxies ionize the IGM as star formation proceeds. In a one-zone approximation, we estimate time evolution of cosmic ionization degree (Barkana & Loeb 2001),

$$\frac{dQ_{\text{HII}}}{dt} = \frac{1}{n_{\text{H}}^0} \dot{n}_{\text{ion}}^\gamma f_{\text{esc, ion}} - \alpha_{\text{B}} C (1+z)^3 n_{\text{H}}^0 Q_{\text{HII}}, \quad (2)$$

where Q_{HII} is the volume fraction of HII, n_{H}^0 is the present-day hydrogen number density ($\sim 2 \times 10^{-7} \text{ cm}^{-3}$), $\dot{n}_{\text{ion}}^\gamma$ is the intrinsic ionizing photon emissivity per unit volume, α_{B} is the case-B recombination rate, C is a clumpiness factor of IGM, and $f_{\text{esc, ion}}$ is escape fraction of ionizing photons, which is a free parameter here. We

estimate $\dot{n}_{\text{ion}}^\gamma$ from star formation history of each halo by using Starburst99 with the Salpeter initial mass function with the metallicity of $10^{-2} Z_\odot$. The reionization history is shown in the upper panel of Figure 3. As $f_{\text{esc,ion}}$ increases, the IGM is ionized earlier. We assume the recombination rate for $T = 10^4$ K ($\alpha_B = 2.6 \times 10^{-13} \text{ cm}^3 \text{ s}^{-1}$) and $C = 3$, as suggested by numerical simulations (Pawlik et al. 2009; Jeon et al. 2014).

The cosmic reionization history is regulated by $f_{\text{esc,ion}}$. Free electrons produced by the cosmic reionization contribute to the Thomson scattering optical depth (τ_e) of CMB photons, defined as

$$\tau_e = \int_0^{z_{\text{rec}}} \sigma_T n_e(z) c \left| \frac{dt}{dz} \right| dz, \quad (3)$$

where $z_{\text{rec}} = 1100$ is the redshift at the time of recombination. In this work, we assume the single ionization fraction of helium is the same as the one for hydrogen at $z \geq 3$, and the double ionization takes place at $z < 3$ (e.g., Wyithe et al. 2010; Inoue et al. 2013). Recent simulations show that indeed the fraction of HeII is close to the HII fraction at high redshifts, although the ionization fraction of helium is slightly lower than the one for hydrogen (Ciardi et al. 2012). The top panel of Figure 3 represents the ionization history of hydrogen gas with the different $f_{\text{esc,ion}}$. The bottom panel of Figure 3 shows τ_e with different $f_{\text{esc,ion}}$. The Thomson scattering optical depth τ_e increases with redshift in a way depending on $f_{\text{esc,ion}}$ due to the different ionization histories. We find $f_{\text{esc,ion}} = 0.2$ nicely reproduces the CMB observation (Planck 2016). Therefore, in this work, we adopt $f_{\text{esc,ion}} = 0.2$ with no redshift evolution. In fact, Yajima et al. (2014) showed $f_{\text{esc,ion}}$ is constant with redshift and ~ 0.2 by cosmological simulations with radiative transfer calculations.

3. RESULTS

3.1. Evolution of ionized bubbles around galaxies

We follow the growth history of HII bubbles around individual galaxies with the star formation efficiency α and $f_{\text{esc,ion}}$ estimated above. Sizes of HII bubbles evolve with ionizing photon emissions, recombination, and cosmic expansion as follows (Cen & Haiman 2000):

$$\frac{dR_{\text{HII}}^3}{dt} = 3H(z)R_{\text{HII}}^3 + \frac{3\dot{N}_{\text{ion}}^\gamma f_{\text{esc,ion}}}{4\pi n_{\text{H}}(z)} - Cn_{\text{H}}(z)\alpha_B R_{\text{HII}}^3, \quad (4)$$

where $H(z)$ is the Hubble constant at specific redshifts, and $\dot{N}_{\text{ion}}^\gamma$ is intrinsic ionizing photon emissivity of each galaxy. The ionizing fronts can propagate up to the Strömgren radius during the recombination time scale (Spitzer 1978). The recombination time scale is $t_{\text{rec}} \sim \frac{1}{\alpha_B n_{\text{H}}} \sim 0.5 \text{ Gyr} \left(\frac{1+z}{11}\right)^{-3}$, which is longer than the typical time scale over which SFR changes more than factor ~ 2 . Therefore, HII bubbles do not reach the equilibrium state, and we need to consider SFR history to estimate the sizes of HII bubbles at given redshifts. We estimate probability distribution function (PDF) of the sizes of ionized bubbles (R_{HII}) as shown in Figure 4. In our model, higher mass halos tend to possess larger ionized bubbles. Due to the decrease in the number density of halos on the high-mass end of a halo

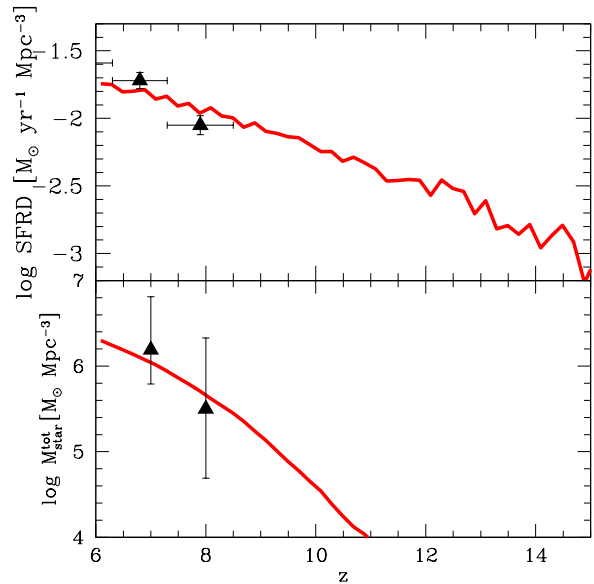


Figure 1. Upper panel: Star formation rate density. Red line represents our modeled star formation history based on the halo merger trees. Triangle symbols show the observation by Bouwens et al. (2015). The observed star formation rate densities are estimated by integrating the luminosity functions in the range of $M_{\text{UV}} \leq -17$. Our model also consider only the galaxies brighter than the same limiting magnitude. Lower panel: Stellar mass density. Red line is the cumulated stellar mass of our model considering only the galaxies with $M_{\text{star}} \geq 10^8 M_\odot$. Triangle symbols show the observation by Song et al. (2016a), who integrated the derived stellar mass functions for galaxies with $M_{\text{star}} \geq 10^8 M_\odot$.

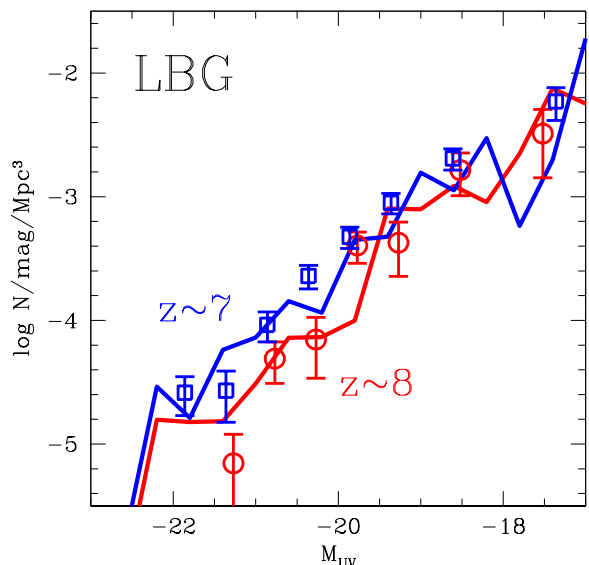


Figure 2. UV luminosity functions. Open squares and circles represent observed LBGs at $z \sim 7$ and ~ 8 by Bouwens et al. (2015).

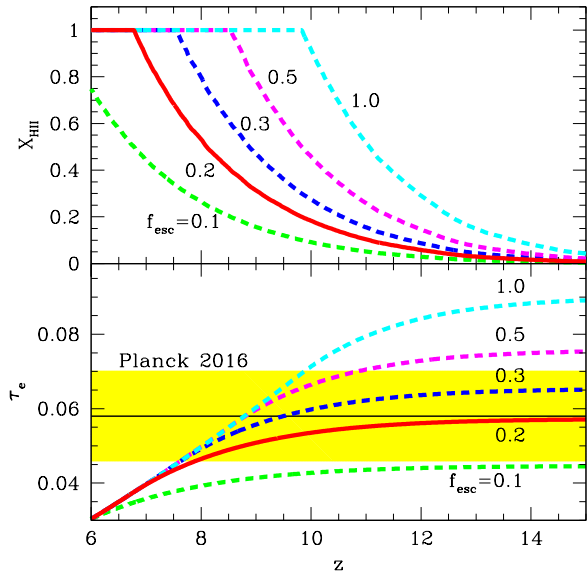


Figure 3. Upper panel: Ionization history. Different lines show ionization histories with different escape fractions of ionizing photons. Lower panel: Thomson scattering optical depth. Different lines are estimated with different ionization histories presented in the upper panel. Yellow shade represents the estimation by the CMB observation (Planck Collaboration et al. 2016).

mass function (Sheth & Tormen 2002), the PDF of R_{HII} rapidly decreases at larger R_{HII} . Although the ionizing front does not reach the size of Strömgren sphere $r_{\text{st}} \propto (\dot{N}_{\text{ion}}^\gamma)^{1/3} (1+z)^{-2}$, it can be used as a rough indicator of sizes of HII bubbles. As redshift decreases, the IGM density decreases while the number density of massive halos with higher ionizing photon emissivity increases. Therefore, the tail of PDF in the large- R_{HII} end shifts to larger R_{HII} at lower redshift. Future 21 cm observations, e.g., SKA-2, is supposed to probe the IGM ionization structure with the angular resolution of $\sim 1'$. Therefore, at $z \lesssim 10$, the tail of PDF at large R_{HII} can be observationally investigated in future. The halo number density monotonically increases as the halo mass decreases at a fixed redshift. Since the size of HII bubble is positively related with halo mass as will be shown in Section 3.3, it seems that the PDFs in the small- R_{HII} end monotonically increase as R_{HII} decreases. However, there are peaks in the PDFs, below which they decrease as R_{HII} decreases. This is caused by the threshold of halo mass for star formation imposed in this work.

3.2. Ly α luminosity functions

Absorption of ionizing photons by interstellar medium within galaxies results in Ly α emissions via recombination processes, while escaped photons cause the cosmic reionization as shown in the previous section. The Ly α luminosity ($L_{\text{Ly}\alpha}$) is estimated by

$$L_{\text{Ly}\alpha} = 0.68(1.0 - f_{\text{esc,ion}})f_{\text{esc,Ly}\alpha}\epsilon_{\text{Ly}\alpha}\dot{N}_{\text{ion}}^\gamma, \quad (5)$$

where $f_{\text{esc,Ly}\alpha}$ is the escape fraction of Ly α photons from galaxies, $\epsilon_{\text{Ly}\alpha} = 10.2$ eV is the energy of a Ly α photon. The escape fraction of Ly α photons $f_{\text{esc,Ly}\alpha}$ can be lower than $f_{\text{esc,UV}}$ because the path length of Ly α photons until escape can be longer due to multiple

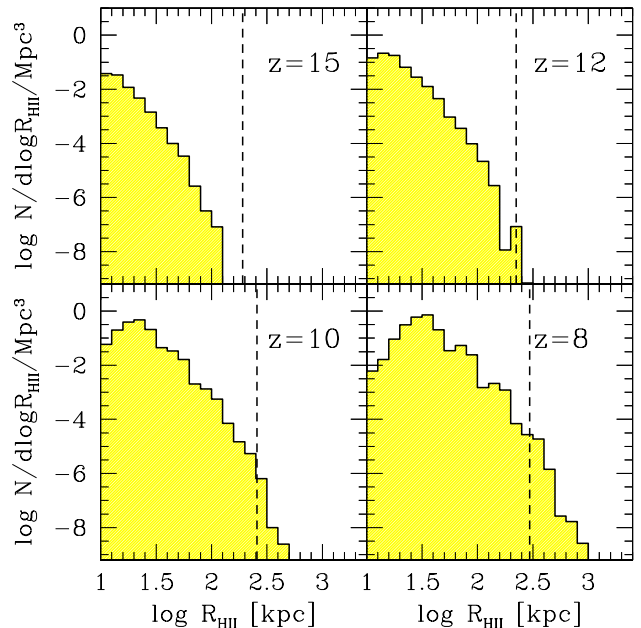


Figure 4. Probability distribution functions of sizes of HII bubbles associated with individual galaxies. Vertical dash lines are corresponding to the viewing angle of 1 arcmin.

scattering process. However, if dust mainly distributes in HI gas clumps, $f_{\text{esc,Ly}\alpha}$ does not become lower than $f_{\text{esc,UV}}$ because Ly α photons are scattered by hydrogen on surface of the clumps before interacting with dust. Ciardullo et al. (2012) indicated that $f_{\text{esc,Ly}\alpha} \sim f_{\text{esc,UV}}$ for observed LAEs at $z \sim 2$. In addition, cosmological simulations of Yajima et al. (2014) showed that $f_{\text{esc,Ly}\alpha}$ was $\gtrsim 0.6$ and similar to $f_{\text{esc,UV}}$ at $z \gtrsim 6$. Therefore, in this work, we assume that $f_{\text{esc,Ly}\alpha} = f_{\text{esc,UV}} = 0.6$.

Next, we estimate IGM transmission as a function of wavelength. As in Cen & Haiman (2000), we divide the paths along which Ly α photons travel from galaxies to us into the two parts, i.e., outside and inside ionized bubbles, and separately estimate each contribution. The transmission outside ionized bubbles is estimated as follows:

$$\tau(\lambda_{\text{obs}}, z_s) = \int_{z_r}^{z_i} dz c \frac{dt}{dz} n_{\text{H}}(z) x_{\text{HI}} \sigma_{\text{Ly}\alpha} [\lambda_{\text{obs}} / (1+z)], \quad (6)$$

where $z_i \sim z_s - \frac{R_{\text{HII}} \times (1+z)}{R_{\text{H}}}$. Here, z_r is redshift when the cosmic reionization completes, which we set $z_r = 6$, z_i is redshift when Ly α photons pass through ionizing front, z_s is redshift of galaxy, $\sigma_{\text{Ly}\alpha}$ is the scattering cross section for HI gas, R_{H} is the size of the cosmological horizon at z_s . We assume the outside of the bubble is completely neutral, i.e., $x_{\text{HI}} = 1$. The $\sigma_{\text{Ly}\alpha}$ is estimated by (Verhamme et al. 2006)

$$\sigma_{\text{Ly}\alpha}[\lambda] = 1.041 \times 10^{-13} \left(\frac{T}{10^4 \text{ K}} \right)^{-\frac{1}{2}} \frac{H(x, a)}{\sqrt{\pi}}. \quad (7)$$

We set $T = 10^4$ K in this work. Here, $H(x, a)$ is the Voigt function,

$$H(x, a) = \frac{a}{\pi} \int_{-\infty}^{+\infty} \frac{e^{-y^2}}{(x-y)^2 + a^2} dy \quad (8)$$

where $x \equiv (\nu - \nu_0)/\Delta\nu_D$, $\nu_0 = 2.466 \times 10^{15}$ Hz is the line-center frequency, ν_D is the Doppler width, $a = \Delta\nu_L/(2\Delta\nu_D)$, $\Delta\nu_L = 9.936 \times 10^7$ Hz is the natural line width. We here use the fitting formula of $H(x, a)$ given by Tasitsiomi (2006).

Even inside ionized bubbles, a tiny fraction of neutral hydrogens exist. We estimate the IGM transmission from ionizing front to virial radius with the neutral fraction under the ionization equilibrium state,

$$x_{\text{HI}} = 1.5 \times 10^{-5} \left(\frac{C}{3}\right) \left(\frac{r}{\text{kpc}}\right)^2 \left(\frac{\dot{N}_{\text{ion}}^\gamma}{10^{50} \text{ s}^{-1}}\right)^{-1} \left(\frac{1+z}{8}\right)^3. \quad (9)$$

Note that, the optical depth outside the ionized bubble is dominant in our work. The IGM transmission is mostly almost zero at $\lambda \lesssim \lambda_0$, where $\lambda_0 = 1216 \text{ \AA}$ is the wavelength of Ly α line center.

Considering the IGM transmission, we derive Ly α LFs, and compare them with the observation of Konno et al. (2014). Depending on the shape of Ly α line profile, the IGM transmission significantly changes. Even with recent deep spectroscopies, however, it is difficult to determine intrinsic Ly α line profiles, i.e., before the IGM extinction (e.g., Ouchi et al. 2010). The intrinsic Ly α line profile depends on the physical nature of galaxies, e.g., HI column density and velocity field (e.g., Verhamme et al. 2006). In this work, we calculate intrinsic Ly α line profiles by Ly α radiation transfer simulations using the code developed in Yajima et al. (2012b), and study the physical nature of LAEs through the comparison with the observation (Konno et al. 2014). The intrinsic line profiles are calculated based on spherically outflowing gas cloud models with the following velocity structure,

$$V(r) = V_{\text{out}} \left(\frac{r}{R_{\text{edge}}}\right), \quad (10)$$

where R_{edge} is the edge of the spherical cloud and V_{out} is the outflow velocity at R_{edge} . Although the simulated profiles do not depend on R_{edge} , here we consider $R_{\text{edge}} \sim R_{\text{vir}}$. Figure 5 shows the modeled line profiles with various outflowing velocities. The Ly α line profiles get the asymmetric shape with a peak at redder wavelength for the outflow velocity field, because Ly α photons at bluer wavelength are scattered by HI gas due to the Doppler shift. As N_{HI} increases, the line profiles are extended, and the peak frequency shift farther from the line center frequency. For the inflow velocity field, the Ly α line profile becomes the mirror symmetric shape to the one for outflow with the same absolute value of the velocity.

With the simulated intrinsic line profiles, we can estimate Ly α LFs for given N_{HI} and V_{out} . In this work, we infer typical N_{HI} and V_{out} of LAEs by comparing modeled LFs with the observed one by Konno et al. (2014). Figure 6 show the LFs. Here we calculate the LFs for three HI column density models, $N_{\text{HI}} = 2 \times 10^{20} \text{ cm}^{-2}$ (model A), $N_{\text{HI}} = 2 \times 10^{19} \text{ cm}^{-2}$ (model B), and $N_{\text{HI}} = 2 \times 10^{18} \text{ cm}^{-2}$ (model C). The column density of model A is corresponding to Damped Lyman- α Systems (DLAs: Wolfe et al. 2005). Yajima et al. (2012a) showed that DLAs distributed at lines of sight passing star-forming regions in high-redshift star-forming galax-

ies by combining cosmological SPH simulations with radiation transfer calculations. These column densities are optically thick to ionizing photons, hence not consistent with $f_{\text{esc,ion}} = 0.2$. However, recent simulations showed ionizing photons mostly escape along ionized holes created by radiative and SNe feedback (e.g., Yajima et al. 2009, 2011; Kimm & Cen 2014). Thus, $f_{\text{esc,ion}}$ of 20 % can be considered as the fraction of viewing angle along which star forming regions are not covered by HI gas. For simplicity, we do not take account of the effect of such holes on line profiles. Note that, however, Ly α line profiles somewhat change due to the holes, clumpiness or other detailed structure in HI gas (Dijkstra & Kramer 2012).

The shaded regions in Figure 6 represent the LFs using different Ly α line profiles with the velocity range from $V_{\text{out}} = -300 \text{ km s}^{-1}$ to 300 km s^{-1} . The best fit velocities are 180 km s^{-1} (model A), 190 km s^{-1} (model B), and 110 km s^{-1} (model C), as summarized in Table 1. Only model A with the velocity range $V_{\text{out}} \sim 150 - 300 \text{ km s}^{-1}$ can reproduce the observed LF well. Therefore we suggest LAEs are likely to have high HI column density with $\gtrsim 10^{20} \text{ cm}^{-2}$ and outflowing HI gas with velocity $\gtrsim 150 \text{ km s}^{-1}$. The Ly α profile monotonically shifts to redder one as the outflow velocity increases in model A as shown in Figure 5. On the other hand, as the HI column density decreases, the Ly α profile moves back to the line center frequency at specific velocity of $< 300 \text{ km s}^{-1}$. This is because Ly α photons can escape from the cloud before shifting to longer wavelength due to lower optical depth. In this work, the best fit velocities for model B and C roughly correspond to those producing the Ly α profiles shifted farthest away. In addition, the width of line profile becomes smaller as the HI column density decrease. Even with the best fit velocities, the number densities of LAEs in the model B and C are smaller than the observation because of the narrower line profiles resulting in lower IGM transmission. Hence, in order to get higher IGM transmission to reproduce the LF, LAEs are likely to have the column density higher than $\sim 10^{20} \text{ cm}^{-2}$. Thus, in this work, we consider model A as our fiducial model.

Emergent Ly α line profiles are shown in Figure 7. As HI column density decreases, intrinsic Ly α line profiles become narrower and peak positions shift to shorter wavelength. IGM transmission increases with wavelength because photons with long wavelength redshift early to avoid from being scattered by the IGM, while Ly α flux near the line center is reduced efficiently by the IGM scattering. FWHMs of the emergent line profiles are 1.5 \AA (model A), $8.9 \times 10^{-1} \text{ \AA}$ (model B) and $5.2 \times 10^{-2} \text{ \AA}$ (model C). Therefore it is difficult to distinguish the different column density models in the current spectroscopic observation with the resolution of $R \sim 1000 - 2000$ (e.g., Shibuya et al. 2012). Future high-dispersion spectroscopies with $R \gg 2000$, e.g., Prime Focus Spectrograph on Subaru or JWST, will be able to reveal the detailed shape of profile.

Line profiles in inflowing gas models result in the underproduction of observable LAEs, because most of Ly α photons are scattered by the IGM. This is consistent with the observation by Ouchi et al. (2010), which indicated LAEs at $z = 6.6$ are likely to have outflowing gas by the

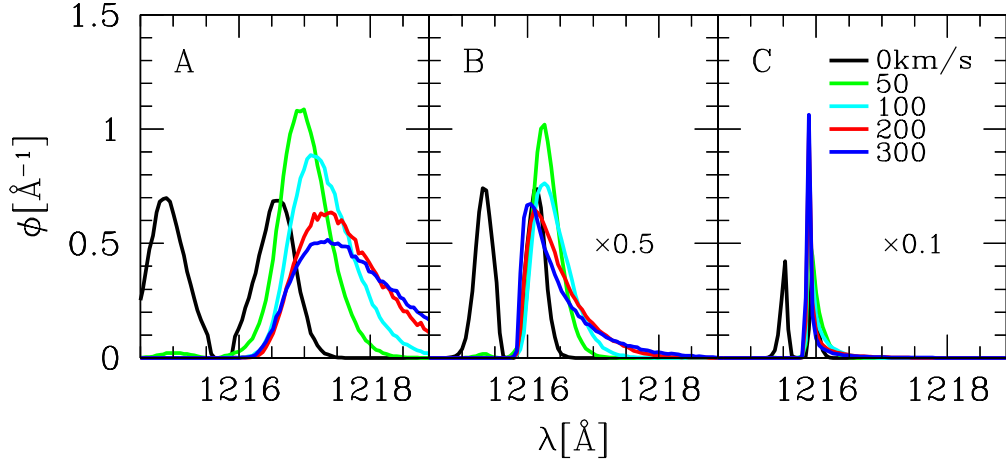


Figure 5. Ly α line profiles from expanding spherical gas clouds with the velocity field as $V(r) = V_{\text{out}} \left(\frac{r}{R_{\text{edge}}} \right)$, where R_{edge} is the radius of clouds and V_{out} is the velocity at R_{edge} . The different panels show the Ly α profiles considering different HI column densities: $N_{\text{HI}} = 2 \times 10^{20} \text{ cm}^{-2}$ (panel A), $2 \times 10^{19} \text{ cm}^{-2}$ (panel B), and $2 \times 10^{18} \text{ cm}^{-2}$ (panel C). The different lines represent the different expanding velocities at R_{edge} . The $\phi(\lambda)$ is normalized to be unity when it is integrated over the wavelength. The $\phi(\lambda)$ of panel (B) and (C) is artificially reduced by a factor 2 and 10.

composite spectrum. In addition, Shibuya et al. (2014) measured outflow velocities of individual LAEs at $z \sim 2$, and indicated that LAEs were likely to have outflow with $V_{\text{out}} \gtrsim 150 \text{ km s}^{-1}$.

Next we estimate the redshift evolution of LF based on the model A with $V_{\text{out}} = 180 \text{ km s}^{-1}$. Figure 8 shows the modeled LFs at $z = 7, 8, 10$ and 12 . Note that, here we use the same line profile for all halos and redshift. At higher redshifts, typical SFR is smaller due to lower halo mass and halo growth rate. In addition, as redshift increases, typical size of HII bubbles decreases, resulting in the lower IGM transmission. As a result, the LF rapidly shifts to the fainter side at higher redshifts.

3.3. Relation between Ly α luminosity and stellar mass

Figure 9 shows the sizes of HII bubbles and Ly α luminosities considering the IGM transmission. Ly α properties are calculated by using the Ly α profile of model A. The shades represent the range of 25%–75% in the sample. We see that R_{HII} tightly correlate with stellar mass, as $R_{\text{HII}} \propto M_{\text{star}}^{1/3}$, while the relation with SFR shows a large dispersion.

SFR rapidly increase by major merger. However, R_{HII} is not so sensitive to the short-time fluctuation of SFR because of the longer time-scale for reaching the ionization equilibrium state. As a result, the relation between R_{HII} and SFR shows the large dispersion. High-redshift galaxies have been observed as so-called Lyman-break galaxies (LBGs: Bouwens et al. 2012), via the Lyman-break technique so far. Our results indicate LBGs at $z \gtrsim 7$ with similar UV brightness can have different Ly α fluxes due to the scatter of IGM transmission. At $z = 15$, our sample is limited by the stellar mass of galaxies $M_{\text{star}} \sim 10^9 M_{\odot}$. In our model, since the stellar mass is simply proportional to halo mass as $M_{\text{star}} \sim 3.3 \times 10^{-3} M_{\text{h}}$, this means that there is no progenitors with $M_{\text{h}} \gtrsim 3 \times 10^{11} M_{\odot}$ at $z = 15$ in our halo sample, which is constructed to have the mass range from 10^9 to $10^{13} M_{\odot}$ at $z = 6$.

In contrast to the SFR- R_{HII} relation, both Ly α lu-

minosity and R_{HII} tightly correlate with M_{star} . The $L_{\text{Ly}\alpha}$ - M_{star} relation does not change with redshift significantly, while the R_{HII} - M_{star} becomes smaller as redshift increases. This is because Hubble constant (i.e., expanding velocity of IGM) becomes large at higher redshift. Therefore, although R_{HII} decreases as redshift increases due to higher IGM density, the IGM transmission does not decrease significantly. Thus, Ly α luminosity does not depend sensitively on redshift.

The detection sensitivity of recent observations of LAEs at $z \sim 7$ – 8 was corresponding to Ly α luminosity of $\gtrsim 3 \times 10^{42} \text{ erg s}^{-1}$ (Ono et al. 2012; Shibuya et al. 2012; Finkelstein et al. 2013; Vanzella et al. 2011; Konno et al. 2014; Zitrin et al. 2015). In our model, median and minimum stellar masses producing $L_{\text{Ly}\alpha} \sim 3 \times 10^{42} \text{ erg s}^{-1}$ at $z = 7.3$ are 6.5×10^9 and $1.5 \times 10^8 M_{\odot}$, respectively. Therefore, by considering the relation $M_{\text{star}} \sim 3.3 \times 10^{-3} M_{\text{h}}$, we suggest that the observed LAEs at $z = 7.3$ should be hosted in halos with $M_{\text{h}} \geq 4.6 \times 10^{10} M_{\odot}$, and the median halo mass is $1.9 \times 10^{12} M_{\odot}$.

3.4. Redshift evolution of number density of observable LAEs

So far the Ly α line has been used as the most strong tool to confirm the redshift of distant galaxy candidates (e.g., Iye et al. 2006; Finkelstein et al. 2013; Zitrin et al. 2015). However, it is widely thought that LAEs at $z > 9$ are difficult to be detected because of the IGM opacity. Here, we estimate the number density of LAEs (n_{LAE}) with higher Ly α flux than specific thresholds. Figure 10 shows the number density of LAEs with $F_{\text{Ly}\alpha} \geq 10^{-17}, 10^{-18}$ and $10^{-19} \text{ erg s}^{-1} \text{ cm}^{-2}$. The detection limits of current observations with a reasonable integration time are $\sim 10^{-17} \text{ erg s}^{-1} \text{ cm}^{-2}$ (e.g., Shibuya et al. 2012). As explained in Sec. 3.2, the number density of bright LAEs monotonically decreases with increasing redshift. Given the detection limits of $10^{-17} \text{ erg s}^{-1} \text{ cm}^{-2}$, wide field surveys of 100^3 Mpc^3 are able to detect LAEs up to $z \sim 8.5$. This is consistent with recent observed LAEs at $z \lesssim 9$ (Finkelstein et al.

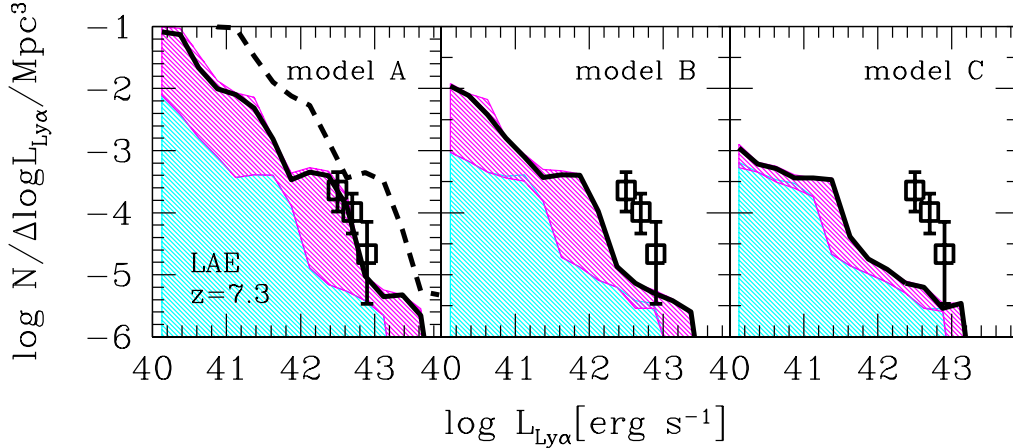


Figure 6. Ly α luminosity functions (LFs) at $z = 7.3$. Square symbols represent the observed LF of LAEs at $z = 7.3$ by Konno et al. (2014). Different panels show modeled LFs based on Ly α line profiles to different HI column densities. Magenta and cyan shades show the range of LFs considering Ly α line profile with different outflow and inflow velocity with the range $0 \sim \pm 300 \text{ km s}^{-1}$. Black solid lines are best fitted ones to the observation. Black dash line in the left panel shows the LF before considering IGM transmission.

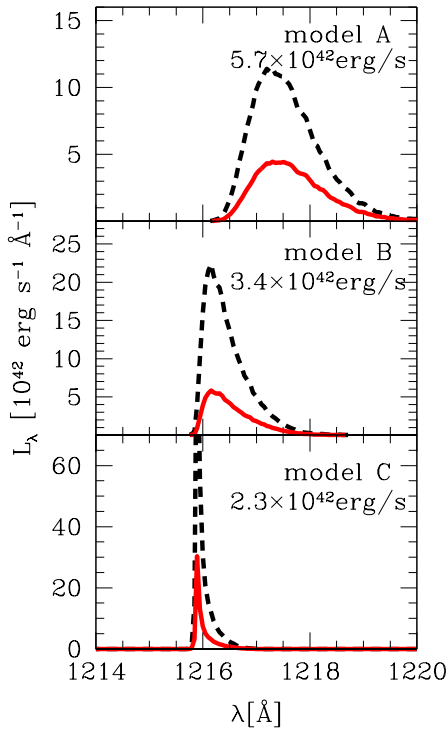


Figure 7. Ly α line profiles. Red solid lines show emergent line profiles of a halo of $5.9 \times 10^{11} M_{\odot}$ at $z=7.3$, which evolves to a halo of $1.0 \times 10^{12} M_{\odot}$ at $z = 6.0$. Intrinsic Ly α luminosity of the halo is $1.3 \times 10^{43} \text{ erg s}^{-1}$. Emergent luminosities after IGM transmission are shown in the panels. Black dash lines are the line profiles before considering IGM transmission.

2013; Oesch et al. 2015; Zitrin et al. 2015). The LAEs with $F_{\text{Ly}\alpha} \geq 10^{-17}$ at $z \sim 10$ are quite rare, with $n_{\text{LAE}} \sim 1 - 2 \text{ Gpc}^{-3}$.

Spectroscopies of next generation telescopes, e.g., JWST, are supposed to achieve the sensitivity of $\sim 10^{-18} \text{ erg s}^{-1} \text{ cm}^{-2}$ with a reasonable integration time. If galaxies at $z \sim 10$ have outflowing gas with $v \gtrsim$

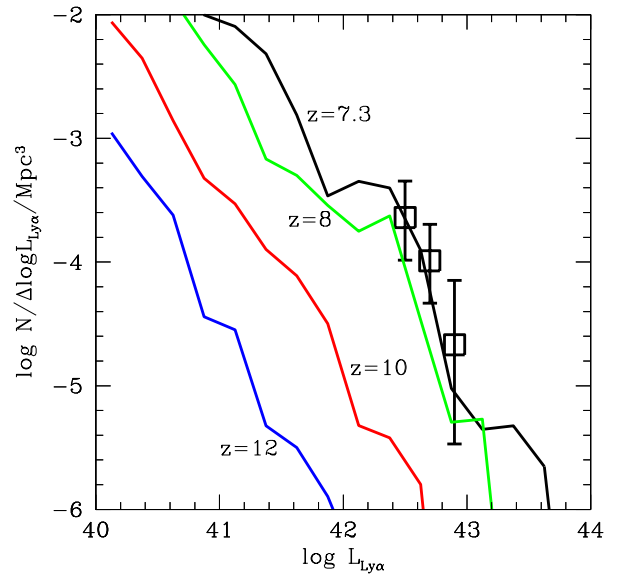


Figure 8. Ly α luminosity functions at $z = 7.3, 8, 10$ and 12 . Open squares show observed LAEs at $z = 7.3$ (Konno et al. 2014).

200 km s^{-1} , the number density of LAEs with $F_{\text{Ly}\alpha} \geq 10^{-18} \text{ erg s}^{-1} \text{ cm}^{-2}$ at $z \sim 10$ is $\sim \text{a few} \times 10^{-6} \text{ Mpc}^{-3}$. As shown in Figure 9, bright LAEs are hosted in massive halos. The median halo and stellar mass of LAEs with $F_{\text{Ly}\alpha} \geq 10^{-18} \text{ erg s}^{-1} \text{ cm}^{-2}$ at $z = 10$ are 1.1×10^{12} and $3.5 \times 10^9 M_{\odot}$, respectively. It was suggested that the observed LBG at $z = 11.1$, GNz11, had the stellar mass of $\sim 10^9 M_{\odot}$ (Oesch et al. 2016), which is corresponding to $F_{\text{Ly}\alpha} \sim 0.2 \times 10^{-18} \text{ erg s}^{-1} \text{ cm}^{-2}$ in our model. Hence, it will be challenging to detect Ly α flux from GNz11 even by future spectroscopies with the line sensitivity of $F_{\text{Ly}\alpha} \sim 10^{-18} \text{ erg s}^{-1} \text{ cm}^{-2}$.

Different line profile models predict different number densities of observable LAEs. The IGM transmission becomes more sensitive to the intrinsic Ly α line profile models, since the typical size of HII bubbles gets smaller

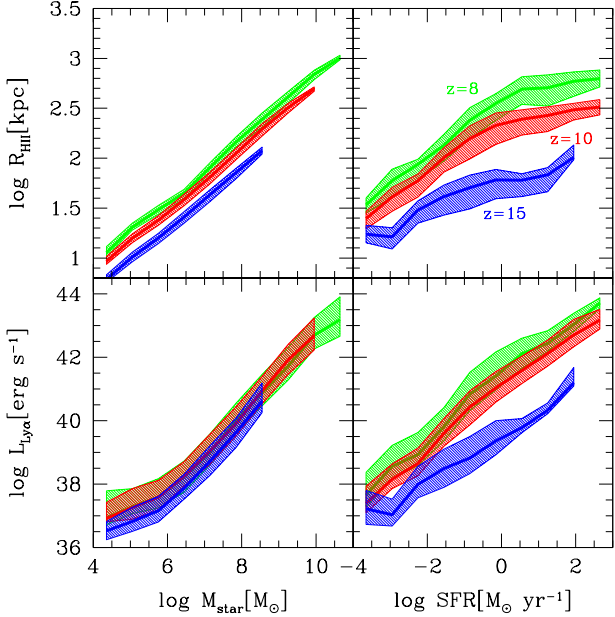


Figure 9. Upper panel: Sizes of HII bubbles as a function of stellar mass and SFR. Green, red and blue lines represent median values to galaxies at $z = 8, 10$ and 15 , respectively. The shades show quartiles at each bin. Lower panel: Ly α luminosity as a function of stellar mass and SFR.

with increasing redshift. As a result, the difference of n_{LAE} among model A, B and C becomes larger at higher redshift, and more than order unity at $z \sim 10$. Future observation would also allow us to discriminate intrinsic line profiles, which in turn provide information about HI column density and outflow velocity, by comparing the observed number density of LAEs with the theoretical models.

Even next generation telescopes, e.g., GMT, E-ELT, TMT, will be difficult to have the sensitivity of $\sim 10^{-19}$ erg s $^{-1}$ cm $^{-2}$. However, if future telescopes somehow achieve such a high sensitivity, wide field surveys of $\sim 100^3$ Mpc 3 would be able to reach LAEs at $z \sim 12$.

In this work, we consider isolated HII bubbles associated with individual LAEs in the estimation of IGM transmission. However, at lower redshift, HII bubbles can be overlapped each other (e.g., Iliev et al. 2012; Hasegawa & Semelin 2013; Ocvirk et al. 2016). The overlapped HII bubbles can enhance the IGM transmission. This effect will be investigated in Hasegawa et al. (in preparation) by combining large-scale N -body with small scale radiative-hydrodynamics simulations.

4. DISCUSSION

4.1. Condition for galactic outflow from LAEs

As shown in Section 3.2, high-redshift LAEs are likely to have galactic wind with $V_{\text{out}} \gtrsim 150$ km s $^{-1}$. Here we roughly derive the condition for making gas outflow with $V_{\text{out}} \gtrsim 150$ km s $^{-1}$ in a spherical gas cloud model. Supernova (SN) feedback can be responsible for causing strong outflow in high-redshift low-mass galaxies (e.g., Kimm & Cen 2014; Kimm et al. 2015). In the assumption that supernovae give feedback to all gas uniformly,

Table 1
Model parameters

| Model | $N_{\text{HI}}/\text{cm}^2$ | $V_{\text{out}}/\text{km s}^{-1}$ |
|---------------------------------|-----------------------------|-----------------------------------|
| A | 2×10^{20} | 180 |
| B | 2×10^{19} | 190 |
| C | 2×10^{18} | 110 |
| $f_{\text{esc,ion}} = 0.2$ | | |
| $f_{\text{esc,UV}} = 0.6$ | | |
| $f_{\text{esc,Ly}\alpha} = 0.6$ | | |

NOTES.—For each HI column density, the outflow velocity is chosen to reproduce the observed luminosity function of LAE at $z = 7.3$ (Konno et al. 2014). Escape fractions of ionizing, UV and Ly α photons are same for all models.

we estimate the total kinetic energy of outflowing gas as

$$\frac{1}{2} M_{\text{gas}} V_{\text{out}}^2 \sim f_{\text{conv}} e_{\text{SN}} N_{\text{SN}} - \frac{GM_{\text{H}} M_{\text{gas}}}{R_{\text{vir}}}. \quad (11)$$

Here $M_{\text{gas}} = (1 - \epsilon) M_{\text{gas}}^0$ is gas mass after star formation, $M_{\text{star}} = \epsilon M_{\text{gas}}^0$ is stellar mass, M_{gas}^0 is initial gas mass, $\epsilon \equiv M_{\text{star}}/M_{\text{gas}}^0$ is a star formation efficiency with respect to the initial gas mass, f_{conv} is the conversion efficiency from total supernova energy to kinetic one of gas, $e_{\text{SN}} \sim 2 \times 10^{51}$ erg is the released energy for each supernova (e.g., Hamuy 2003), and N_{SN} is the number of supernova. For Salpeter-like IMF, $N_{\text{SN}} \sim 1 \times 10^{-2} \frac{M_{\text{star}}}{M_{\odot}} = 1 \times 10^{-2} \left(\frac{\epsilon}{1-\epsilon} \right) \frac{M_{\text{gas}}}{M_{\odot}}$. By using the star formation efficiency ϵ , we simply estimate V_{out} as

$$\sqrt{V_{\text{out}}^2 + v_{\text{esc}}^2} \sim 1.4 \times 10^3 \text{ km s}^{-1} \left(\frac{\epsilon}{1-\epsilon} \right)^{\frac{1}{2}} f_{\text{conv}}^{\frac{1}{2}}, \quad (12)$$

where $v_{\text{esc}} \equiv \sqrt{\frac{2GM_{\text{H}}}{R_{\text{vir}}}}$ is the escape velocity of a halo.

Next we obtain f_{conv} as a function of ϵ . Recently Kim & Ostriker (2015) showed the final momentum produced by a single SN with the energy of 10^{51} erg as follows: $p = 2.8 \times 10^5 \text{ km s}^{-1} M_{\odot} \left(\frac{n_{\text{H}}}{1 \text{ cm}^{-3}} \right)^{-0.17}$ (see also, Cioffi et al. 1988; Thornton et al. 1998). In this work, we ignore the weak density dependence and assume $n_{\text{H}} \sim 1 \text{ cm}^{-3}$. Since the final momentum is almost linearly proportional to the injected SN energy (Cioffi et al. 1988; Kimm & Cen 2014), we approximate the total momentum produced by multiple SNe as follows: $P = p \left(\frac{e_{\text{SN}} N_{\text{SN}}}{10^{51} \text{ erg}} \right)$, where $e_{\text{SN}} N_{\text{SN}}$ is the total energy of supernovae. Therefore, using $E = \frac{P^2}{2M_{\text{gas}}}$, we derive $f_{\text{conv}} = \frac{E}{e_{\text{SN}}} = 16 \left(\frac{\epsilon}{1-\epsilon} \right)$. Note that f_{conv} can not exceed unity according to the energy conservation. For that reason, we set $f_{\text{conv}} = 1$ at $\epsilon \geq 0.06$ because the above expression gives $f_{\text{conv}} > 1$. Thus, Equation 12 is

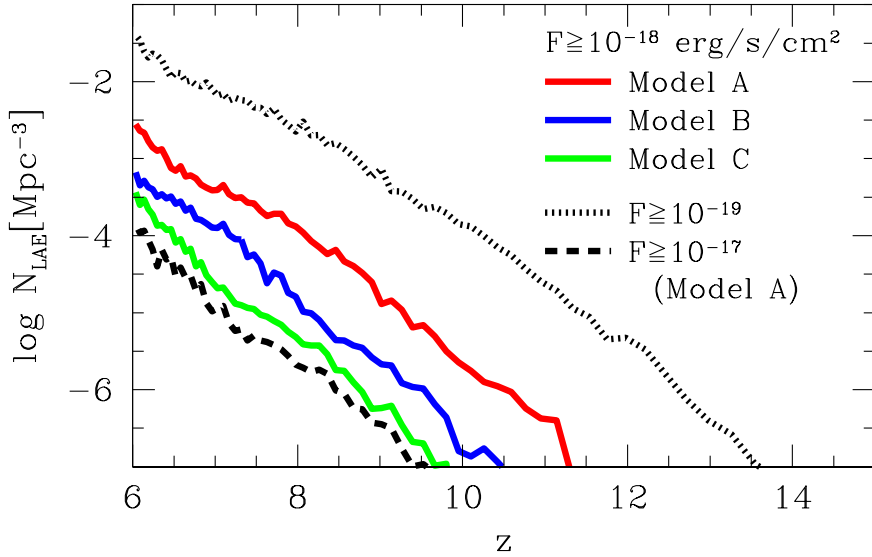


Figure 10. Number density of LAEs as a function of redshift. Red, blue and green lines show the number densities of LAEs with $F_{\text{Ly}\alpha} \geq 10^{-18} \text{ erg cm}^{-2} \text{ s}^{-1}$ obtained assuming Ly α line profiles of model A, B and C, respectively. Black dash and dot lines are the number density of LAEs with $F_{\text{Ly}\alpha} \geq 10^{-17} \text{ erg cm}^{-2} \text{ s}^{-1}$ and $F_{\text{Ly}\alpha} \geq 10^{-19} \text{ erg cm}^{-2} \text{ s}^{-1}$ obtained assuming the Ly α line profile of model A.

written by using ϵ as follows:

$$\sqrt{V_{\text{out}}^2 + v_{\text{esc}}^2} \sim \begin{cases} 5.5 \times 10^3 \text{ km s}^{-1} \left(\frac{\epsilon}{1-\epsilon}\right) & \text{if } \epsilon < 0.06 \\ 1.4 \times 10^3 \text{ km s}^{-1} \left(\frac{\epsilon}{1-\epsilon}\right)^{\frac{1}{2}} & \text{if } \epsilon \geq 0.06. \end{cases} \quad (13)$$

We find that the condition of $\epsilon \sim 0.04$ is required to cause the galactic outflow with $V_{\text{out}} = 180 \text{ km s}^{-1}$ from a halo with $M_{\text{h}} = 4.6 \times 10^{10} M_{\odot}$ at $z = 7.3$ which is minimum halo mass to produce the observable Ly α luminosity $\sim 3 \times 10^{42} \text{ erg s}^{-1}$. We can also convert the tuning parameter α in our star formation model to ϵ , as $\epsilon \sim \alpha \Omega_{\text{M}} / \Omega_{\text{b}} \sim 0.02$. This is roughly similar to the value estimated above. As halo mass increases, higher ϵ is required to cause galactic outflow. Here we have estimated ϵ assuming all gas has same outflow velocity in the simple spherical cloud model. For example, in the case of disk galaxies, only a part of gas can be evacuated along the normal direction to galactic disk as shown in numerical simulations (e.g., Agertz et al. 2011). In this case, strong outflow can be caused even with smaller ϵ because piled gas mass can be lower.

4.2. Relation between Ly α luminosity and size of ionized bubble

LAEs can be responsible for ionizing sources of cosmic reionization (e.g., Yajima et al. 2009, 2011, 2014). Figure 11 shows $L_{\text{Ly}\alpha}$ as a function of the size of associated HII bubble R_{HII} . The Ly α luminosity steeply increases with R_{HII} due to higher IGM transmission for large HII bubbles. The relation between $L_{\text{Ly}\alpha}$ and R_{HII} does not significantly change with redshift. IGM gas density increases with redshift as $\rho \propto (1+z)^3$, resulting in lower IGM transmission at higher redshift. However, galaxies

tend to have higher ionizing photon emissivity and intrinsic Ly α luminosity for a fixed size of HII bubbles at higher redshift. The combination of these effects leads to the weak redshift dependence in the $L_{\text{Ly}\alpha}$ - R_{HII} relation.

The yellow shaded region represents the viewing angle of ≥ 1 arcmin and the flux of $\geq 10^{-18} \text{ erg s}^{-1} \text{ cm}^{-2}$ for $z \sim 10$. This region corresponds to the LAEs with associated HII bubbles that are detectable both as LAEs and holes in 21-cm signal by future galaxy observations by JWST and 21-cm tomography by SKA-2, respectively. Future 21-cm observations will be able to probe giant HII bubbles around bright LAEs with $F_{\text{Ly}\alpha} \gtrsim 10^{-18} \text{ erg s}^{-1} \text{ cm}^{-2}$ at $z \sim 10$.

The differential brightness temperature δT_{b} caused by galaxies shows inner positive and outer negative ring-like structure (e.g., Chen & Miralda-Escudé 2004; Yajima & Li 2014). The detailed structure depends on SED. If galaxies host X-ray sources like AGNs, the positive region is extended due to partial photo-ionization heating. Therefore, future 21-cm observations may also give us information about nature of X-ray and UV sources in bright LAEs.

5. SUMMARY

We present models of Ly α emitting galaxies (LAEs) with IGM transmission considered at the era of reionization. Based on halo merger trees and a simple star formation model, we estimate cosmic star formation and cosmic reionization history. Our model uses 5000 realizations of halo merger trees with the halo mass range from $M_{\text{h}} = 10^9$ to $10^{13} M_{\odot}$ at $z = 6$. As a result, our model reproduces the observed cosmic star formation densities, stellar mass densities, luminosity functions of Lyman-break galaxies with a tuning parameter, $\alpha (\equiv SFR / \frac{dM_{\text{h}}}{dt}) = 3.3 \times 10^{-3}$. Our modeled star formation history, with an escape fraction of ionizing photons $f_{\text{esc,ion}} = 0.2$, also provides a cosmic reionization history

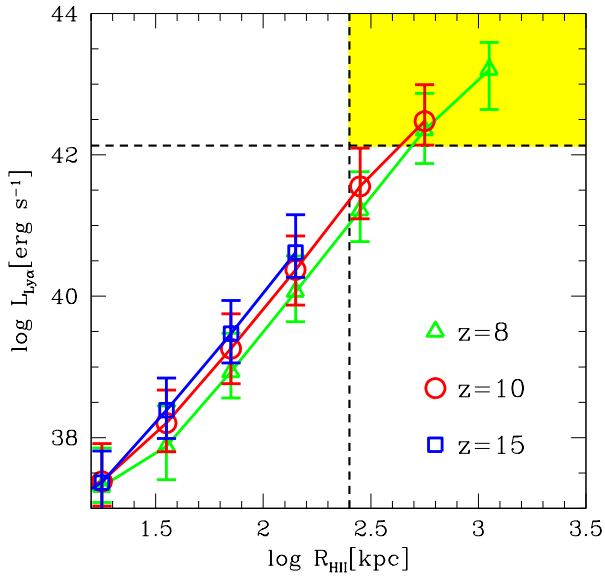


Figure 11. $\text{Ly}\alpha$ luminosity as a function of size of HII bubble. Triangle, circle and square symbols represent median values at $z = 8, 10$ and 15 , respectively. Error bars show quartiles. The $\text{Ly}\alpha$ line profile of model A is used. Horizontal dash line shows $\text{Ly}\alpha$ flux of $10^{-18} \text{ erg cm}^{-2} \text{ s}^{-1}$ for $z = 10$. Vertical dash line represents the viewing angle of 1 arcmin for $z = 10$.

consistent with the Thomson scattering optical depth indicated by Plank (2016).

Based on the above parameters, we model LAEs and HII bubbles using individual halo merger trees. Our models show the distribution function of the size of HII bubble, and indicate giant HII bubbles associated with bright LAEs at $z \lesssim 12$ can be probed by future 21-cm observation using SKA. We find that $\text{Ly}\alpha$ flux is tightly related with stellar/halo mass, while there is a large dispersion in the relation between $\text{Ly}\alpha$ flux and SFR. By comparing our models with the observed luminosity function of LAEs at $z = 7.3$ by Konno et al. (2014), we indicate that LAEs are likely to have the HI column density of $N_{\text{HI}} \gtrsim 10^{20} \text{ cm}^{-2}$ and the outflowing gas with $V_{\text{out}} \gtrsim 150 \text{ km s}^{-1}$. Using these parameters, we predict that future wide deep survey can detect LAEs at $z \sim 10$ with $n_{\text{LAE}} \sim \text{a few} \times 10^{-6} \text{ Mpc}^{-3}$ and $\sim 1 \times 10^{-4} \text{ Mpc}^{-3}$ for the flux sensitivity of $10^{-18} \text{ erg cm}^{-2} \text{ s}^{-1}$ and $10^{-19} \text{ erg cm}^{-2} \text{ s}^{-1}$, respectively. Our models predict next generation telescopes, JWST, E-ELT or TMT would be able to observe galaxies at $z \sim 10$ via the detections of $\text{Ly}\alpha$ lines.

By combining future galaxy observations and 21-cm tomography with SKA-2, we will be able to detect both LAEs with $L_{\text{Ly}\alpha} \gtrsim 10^{42} \text{ erg s}^{-1}$ and their associated giant HII bubbles with $R_{\text{HII}} \gtrsim 250 \text{ kpc}$. We suggest that a clear spatial anti-correlation between galaxies and 21-cm emission will be detected by focusing on such bright LAEs.

ACKNOWLEDGMENTS

We thank Akira Konno and Masami Ouchi for providing us their recent observational data. We are grateful to Masayuki Umemura, Akio Inoue, Yoshiaki Ono, Takatoshi Shibuya, Daisuke Nakauchi and Sadegh Khochfar for valuable discussion and comments. The

numerical simulations were performed on the computer cluster, Draco, at Frontier Research Institute for Interdisciplinary Sciences of Tohoku University. This work is supported in part by MEXT/JSPS KAKENHI Grant Number 15H06022 (HY) and 15J03873 (KS).

REFERENCES

- Agertz, O., Teyssier, R., & Moore, B. 2011, MNRAS, 410, 1391
 Barkana, R., & Loeb, A. 2001, Phys. Rep., 349, 125
 Behroozi, P. S., & Silk, J. 2015, ApJ, 799, 32
 Behroozi, P. S., Wechsler, R. H., & Conroy, C. 2013, ApJ, 770, 57
 Bond, N., Gawiser, E., Guaita, L., Padilla, N., Gronwall, C., Ciardullo, R., & Lai, K. 2011, ArXiv e-prints
 Bouwens, R. J., Illingworth, G. D., Oesch, P. A., Trenti, M., Labbé, I., Bradley, L., Carollo, M., van Dokkum, P. G., Gonzalez, V., Holwerda, B., Franx, M., Spitler, L., Smit, R., & Magee, D. 2015, ApJ, 803, 34
 Bouwens, R. J., Illingworth, G. D., Oesch, P. A., Trenti, M., Labbé, I., Franx, M., Stiavelli, M., Carollo, C. M., van Dokkum, P., & Magee, D. 2012, ApJ, 752, L5
 Cen, R. 2003, ApJ, 591, 12
 Cen, R., & Haiman, Z. 2000, ApJ, 542, L75
 Chen, X., & Miralda-Escudé, J. 2004, ApJ, 602, 1
 Ciardi, B., Bolton, J. S., Maselli, A., & Graziani, L. 2012, MNRAS, 423, 558
 Ciardullo, R., Gronwall, C., Wolf, C., McCathran, E., Bond, N. A., Gawiser, E., Guaita, L., Feldmeier, J. J., Treister, E., Padilla, N., Francke, H., Matković, A., Altmann, M., & Herrera, D. 2012, ApJ, 744, 110
 Cioffi, D. F., McKee, C. F., & Bertschinger, E. 1988, ApJ, 334, 252
 Dewdney, P. E., Hall, P. J., Schilizzi, R. T., & Lazio, T. J. L. W. 2009, IEEE Proceedings, 97, 1482
 Dijkstra, M., & Kramer, R. 2012, MNRAS, 424, 1672
 Fan, X., Carilli, C. L., & Keating, B. 2006, ARA&A, 44, 415
 Finkelstein, S. L., Papovich, C., Dickinson, M., Song, M., Tilvi, V., Koekemoer, A. M., Finkelstein, K. D., Mobasher, B., Ferguson, H. C., Giavalisco, M., Reddy, N., Ashby, M. L. N., Dekel, A., Fazio, G. G., Fontana, A., Grogin, N. A., Huang, J.-S., Kocevski, D., Rafelski, M., Weiner, B. J., & Willner, S. P. 2013, Nature, 502, 524
 Gawiser, E., Francke, H., Lai, K., Schawinski, K., Gronwall, C., Ciardullo, R., Quadri, R., Orsi, A., Barrientos, L. F., Blanc, G. A., Fazio, G., Feldmeier, J. J., Huang, J.-s., Infante, L., Lira, P., Padilla, N., Taylor, E. N., Treister, E., Urry, C. M., van Dokkum, P. G., & Virani, S. N. 2007, ApJ, 671, 278
 Gronwall, C., Ciardullo, R., Hickey, T., Gawiser, E., Feldmeier, J. J., van Dokkum, P. G., Urry, C. M., Herrera, D., Lehmer, B. D., Infante, L., Orsi, A., Marchesini, D., Blanc, G. A., Francke, H., Lira, P., & Treister, E. 2007, ApJ, 667, 79
 Hamuy, M. 2003, ApJ, 582, 905
 Harker, G., Zaroubi, S., Bernardi, G., Brentjens, M. A., de Bruyn, A. G., Ciardi, B., Jelić, V., Koopmans, L. V. E., Labropoulos, P., Mellema, G., Offringa, A., Pandey, V. N., Pawlik, A. H., Schaye, J., Thomas, R. M., & Yatawatta, S. 2010, MNRAS, 405, 2492
 Hasegawa, K., & Semelin, B. 2013, MNRAS, 428, 154
 Hu, E. M., & McMahon, R. G. 1996, Nature, 382, 231
 Iliiev, I. T., Mellema, G., Pen, U.-L., Merz, H., Shapiro, P. R., & Alvarez, M. A. 2006, MNRAS, 369, 1625
 Iliiev, I. T., Mellema, G., Shapiro, P. R., Pen, U.-L., Mao, Y., Koda, J., & Ahn, K. 2012, MNRAS, 423, 2222
 Inoue, Y., Inoue, S., Kobayashi, M. A. R., Makiya, R., Niino, Y., & Totani, T. 2013, ApJ, 768, 197
 Iye, M., Ota, K., Kashikawa, N., Furusawa, H., Hashimoto, T., Hattori, T., Matsuda, Y., Morokuma, T., Ouchi, M., & Shimasaku, K. 2006, Nature, 443, 186
 Jeon, M., Pawlik, A. H., Bromm, V., & Milosavljević, M. 2014, MNRAS, 440, 3778
 Kashikawa, N., Shimasaku, K., Malkan, M. A., Doi, M., Matsuda, Y., Ouchi, M., Taniguchi, Y., Ly, C., Nagao, T., Iye, M., Motohara, K., Murayama, T., Murozono, K., Nariai, K., Ohta, K., Okamura, S., Sasaki, T., Shioya, Y., & Umemura, M. 2006, ApJ, 648, 7

- Khochfar, S., & Burkert, A. 2001, *ApJ*, 561, 517
— 2006, *A&A*, 445, 403
- Kim, C.-G., & Ostriker, E. C. 2015, *ApJ*, 802, 99
- Kimm, T., & Cen, R. 2014, *ApJ*, 788, 121
- Kimm, T., Cen, R., Rosdahl, J., & Yi, S. 2015, *ArXiv e-prints*
- Komatsu, E., Smith, K. M., Dunkley, J., Bennett, C. L., Gold, B., Hinshaw, G., Jarosik, N., Larson, D., Nolte, M. R., Page, L., Spergel, D. N., Halpern, M., Hill, R. S., Kogut, A., Limon, M., Meyer, S. S., Odegard, N., Tucker, G. S., Weiland, J. L., Wollack, E., & Wright, E. L. 2011, *ApJS*, 192, 18
- Konno, A., Ouchi, M., Ono, Y., Shimasaku, K., Shibuya, T., Furusawa, H., Nakajima, K., Naito, Y., Momose, R., Yuma, S., & Iye, M. 2014, *ApJ*, 797, 16
- Kravtsov, A., Vikhlinin, A., & Meshcheryakov, A. 2014, *ArXiv e-prints*
- Lidz, A., Zahn, O., Furlanetto, S. R., McQuinn, M., Hernquist, L., & Zaldarriaga, M. 2009, *ApJ*, 690, 252
- Lonsdale, C. J., Cappallo, R. J., Morales, M. F., Briggs, F. H., Benkevitch, L., Bowman, J. D., Bunton, J. D., Burns, S., Corey, B. E., Desouza, L., Doeleman, S. S., Derome, M., Deshpande, A., Gopala, M. R., Greenhill, L. J., Herne, D. E., Hewitt, J. N., Kamini, P. A., Kasper, J. C., Kincaid, B. B., Kocz, J., Kowald, E., Kratzenberg, E., Kumar, D., Lynch, M. J., Madhavi, S., Matejek, M., Mitchell, D. A., Morgan, E., Oberoi, D., Ord, S., Pathikulangara, J., Prabu, T., Rogers, A., Roshi, A., Salah, J. E., Sault, R. J., Shankar, N. U., Srivani, K. S., Stevens, J., Tingay, S., Vaccarella, A., Waterson, M., Wayth, R. B., Webster, R. L., Whitney, A. R., Williams, A., & Williams, C. 2009, *IEEE Proceedings*, 97, 1497
- Madau, P., & Haardt, F. 2015, *ApJ*, 813, L8
- Madau, P., Haardt, F., & Rees, M. J. 1999, *ApJ*, 514, 648
- Mellema, G., Iliiev, I. T., Pen, U.-L., & Shapiro, P. R. 2006, *MNRAS*, 372, 679
- Mori, M., & Umemura, M. 2006, *Nature*, 440, 644
- Moster, B. P., Naab, T., & White, S. D. M. 2013, *MNRAS*, 428, 3121
- Ocvirk, P., Gillet, N., Shapiro, P. R., Aubert, D., Iliiev, I. T., Teyssier, R., Yepes, G., Choi, J.-H., Sullivan, D., Knebe, A., Gottlöber, S., D'Aloisio, A., Park, H., Hoffman, Y., & Stranex, T. 2016, *MNRAS*, 463, 1462
- Oesch, P. A., Brammer, G., van Dokkum, P. G., Illingworth, G. D., Bouwens, R. J., Labbé, I., Franx, M., Momcheva, I., Ashby, M. L. N., Fazio, G. G., Gonzalez, V., Holden, B., Magee, D., Skelton, R. E., Smit, R., Spitler, L. R., Trenti, M., & Willner, S. P. 2016, *ApJ*, 819, 129
- Oesch, P. A., van Dokkum, P. G., Illingworth, G. D., Bouwens, R. J., Momcheva, I., Holden, B., Roberts-Borsani, G. W., Smit, R., Franx, M., Labbé, I., González, V., & Magee, D. 2015, *ApJ*, 804, L30
- Okamoto, T., Gao, L., & Theuns, T. 2008, *MNRAS*, 390, 920
- Ono, Y., Ouchi, M., Mobasher, B., Dickinson, M., Penner, K., Shimasaku, K., Weiner, B. J., Kartaltepe, J. S., Nakajima, K., Nayyeri, H., Stern, D., Kashikawa, N., & Spinrad, H. 2012, *ApJ*, 744, 83
- Ouchi, M., Shimasaku, K., Akiyama, M., Simpson, C., Saito, T., Ueda, Y., Furusawa, H., Sekiguchi, K., Yamada, T., Kodama, T., Kashikawa, N., Okamura, S., Iye, M., Takata, T., Yoshida, M., & Yoshida, M. 2008, *ApJS*, 176, 301
- Ouchi, M., Shimasaku, K., Furusawa, H., Saito, T., Yoshida, M., Akiyama, M., Ono, Y., Yamada, T., Ota, K., Kashikawa, N., Iye, M., Kodama, T., Okamura, S., Simpson, C., & Yoshida, M. 2010, *ApJ*, 723, 869
- Paardekooper, J.-P., Khochfar, S., & Dalla Vecchia, C. 2013, *MNRAS*, 429, L94
- Pawlik, A. H., Schaye, J., & van Scherpenzeel, E. 2009, *MNRAS*, 394, 1812
- Planck Collaboration, Ade, P. A. R., Aghanim, N., Armitage-Caplan, C., Arnaud, M., Ashdown, M., Atrio-Barandela, F., Aumont, J., Baccigalupi, C., Banday, A. J., & et al. 2014, *A&A*, 571, A16
- Planck Collaboration, Ade, P. A. R., Aghanim, N., Arnaud, M., Ashdown, M., Aumont, J., Baccigalupi, C., Banday, A. J., Barreiro, R. B., Bartlett, J. G., & et al. 2016, *A&A*, 594, A13
- Razoumov, A. O., & Sommer-Larsen, J. 2010, *ApJ*, 710, 1239
- Richards, G. T., Strauss, M. A., Fan, X., Hall, P. B., Jester, S., Schneider, D. P., Vanden Berk, D. E., Stoughton, C., Anderson, S. F., Brunner, R. J., Gray, J., Gunn, J. E., Ivezić, Ž., Kirkland, M. K., Knapp, G. R., Loveday, J., Meiksin, A., Pope, A., Szalay, A. S., Thakar, A. R., Yanny, B., York, D. G., Barentine, J. C., Brewington, H. J., Brinkmann, J., Fukugita, M., Harvanek, M., Kent, S. M., Kleinman, S. J., Krziesiński, J., Long, D. C., Lupton, R. H., Nash, T., Neilsen, Jr., E. H., Nitta, A., Schlegel, D. J., & Snedden, S. A. 2006, *AJ*, 131, 2766
- Robertson, B. E., Ellis, R. S., Furlanetto, S. R., & Dunlop, J. S. 2015, *ApJ*, 802, L19
- Sheth, R. K., & Tormen, G. 2002, *MNRAS*, 329, 61
- Shibuya, T., Kashikawa, N., Ota, K., Iye, M., Ouchi, M., Furusawa, H., Shimasaku, K., & Hattori, T. 2012, *ApJ*, 752, 114
- Shibuya, T., Ouchi, M., Nakajima, K., Hashimoto, T., Ono, Y., Rauch, M., Gauthier, J.-R., Shimasaku, K., Goto, R., Mori, M., & Umemura, M. 2014, *ApJ*, 788, 74
- Somerville, R. S., & Kolatt, T. S. 1999, *MNRAS*, 305, 1
- Song, M., Finkelstein, S. L., Ashby, M. L. N., Grazian, A., Lu, Y., Papovich, C., Salmon, B., Somerville, R. S., Dickinson, M., Duncan, K., Faber, S. M., Fazio, G. G., Ferguson, H. C., Fontana, A., Guo, Y., Hathi, N., Lee, S.-K., Merlin, E., & Willner, S. P. 2016a, *ApJ*, 825, 5
- Song, M., Finkelstein, S. L., Livermore, R. C., Capak, P. L., Dickinson, M., & Fontana, A. 2016b, *ApJ*, 826, 113
- Spitzer, L. 1978, *Physical processes in the interstellar medium*, ed. Spitzer, L.
- Steidel, C. C., Adelberger, K. L., Shapley, A. E., Pettini, M., Dickinson, M., & Giavalisco, M. 2000, *ApJ*, 532, 170
- Tasitsiomi, A. 2006, *ApJ*, 648, 762
- Thornton, K., Gaudlitz, M., Janka, H.-T., & Steinmetz, M. 1998, *ApJ*, 500, 95
- Trac, H., & Cen, R. 2007, *ApJ*, 671, 1
- Vanzella, E., Pentericci, L., Fontana, A., Grazian, A., Castellano, M., Boutsia, K., Cristiani, S., Dickinson, M., Gallozzi, S., Giallongo, E., Giavalisco, M., Maiolino, R., Moorwood, A., Paris, D., & Santini, P. 2011, *ApJ*, 730, L35
- Verhamme, A., Schaerer, D., Atek, H., & Tapken, C. 2008, *A&A*, 491, 89
- Verhamme, A., Schaerer, D., & Maselli, A. 2006, *A&A*, 460, 397
- Wolfe, A. M., Gawiser, E., & Prochaska, J. X. 2005, *ARA&A*, 43, 861
- Wyithe, J. S. B., Hopkins, A. M., Kistler, M. D., Yüksel, H., & Beacom, J. F. 2010, *MNRAS*, 401, 2561
- Yajima, H., Choi, J.-H., & Nagamine, K. 2011, *MNRAS*, 412, 411
— 2012a, *MNRAS*, 427, 2889
- Yajima, H., & Khochfar, S. 2015, *MNRAS*, 448, 654
- Yajima, H., & Li, Y. 2014, *MNRAS*, 445, 3674
- Yajima, H., Li, Y., Zhu, Q., & Abel, T. 2012b, *MNRAS*, 424, 884
- Yajima, H., Li, Y., Zhu, Q., Abel, T., Gronwall, C., & Ciardullo, R. 2014, *MNRAS*, 440, 776
- Yajima, H., Umemura, M., Mori, M., & Nakamoto, T. 2009, *MNRAS*, 398, 715
- Yamada, T., Nakamura, Y., Matsuda, Y., Hayashino, T., Yamauchi, R., Morimoto, N., Kousai, K., & Umemura, M. 2012, *AJ*, 143, 79
- Yoshiura, S., Hasegawa, K., Ichiki, K., Tashiro, H., Shimabukuro, H., & Takahashi, K. 2016, *ArXiv e-prints*
- Zitrin, A., Labbé, I., Belli, S., Bouwens, R., Ellis, R. S., Roberts-Borsani, G., Stark, D. P., Oesch, P. A., & Smit, R. 2015, *ApJ*, 810, L12